Journal of Inorganic and Organometallic Polymers and Materials
https://doi.org/10.1007/s10904-023-02881-9

RESEARCH

An Ab Initio Investigation of the Structural Stability, Thermodynamic, Optoelectronic, and Thermoelectric Properties of $LuXNi_2Sn_2$ (X = V, Nb, Ta) Double Half Heusler Materials

Saber Saad Essaoud[1,2] · Abdelmadjid Bouhemadou[3] · Djamel Allali[4,5] · Mohammed Elamin Ketfi[6] · Missoum Radjai[7] · Saad Bin-Omran[8]

Received: 13 July 2023 / Accepted: 14 September 2023

Abstract

The primary objective of this study is to investigate the influence of spin-orbit coupling and atom type on the electronic, optical, and thermoelectric properties of $LuXNi_2Sn_2$ (X = V, Nb, and Ta) double-half Heusler alloys. To achieve this, calculations were performed using the full potential linearized augmented plane wave method within the framework of density functional theory. Both full relativistic and scalar relativistic calculations were employed. The exchange-correlation interactions in this study were modeled using the PBEsol version of the generalized gradient approximation when calculating the structural ground state parameters. For the analysis of electronic, optical, and thermoelectric properties, the modified Becke–Johnson potential was employed. The modified Becke–Johnson potential was specifically chosen for its capability to improve the description of band gaps, particularly for systems with small band gaps, such as the $LuXNi_2Sn_2$ (X = V, Nb, and Ta) double-half Heusler materials examined in this study. This potential offers a more accurate representation of the electronic properties, enabling a more reliable analysis of the optical and thermoelectric characteristics of the materials under investigation. The examined $LuXNi_2Sn_2$ (X = V, Nb, and Ta) materials exhibit semiconductor behaviour, with band gaps smaller than 0.4 eV that can be controlled by varying the "X" atom. The charge carriers, specifically holes and electrons, exhibit light effective masses, indicating high mobility. Furthermore, these compounds exhibit low thermal expansion coefficients and satisfy the criteria for thermodynamic stability. In terms of optical properties, they display substantial absorption coefficients in the ultraviolet (UV) light region, high optical conductivity, and high reflectivity in the visible light region. Considering their favourable power factor and figure of merit characteristics, the $LuXNi_2Sn_2$ (X = V, Nb, and Ta) materials possess the potential to be promising candidates for thermoelectric applications.

Keywords Double-half Heusler · Ab initio calculation · Spin-orbit coupling · Optical coefficients · Thermoelectricity · Lattice thermal conductivity

✉ Saber Saad Essaoud
saber.saadessaoud@univ-msila.dz

[1] Department of Physics, Faculty of Science, University of M'sila, 28000 M'sila, Algeria

[2] Laboratoire de Physique des Particules et Physique Statistique, Ecole Normale Supérieure-Kouba, BP 92, Vieux-Kouba, 16050 Algiers, Algeria

[3] Laboratory for Developing New Materials and their Characterizations, Department of Physics, Faculty of Science, Ferhat Abbas University - Setif 1, 19000 Setif, Algeria

[4] Physics and Chemistry of Materials Lab, Department of Physics, University of M'sila, 28000 M'sila, Algeria

[5] Faculty of Technology, University of M'sila, B.P. 166, Ichbilia, 28000 M'sila, Algeria

[6] Department of Electronics, Faculty of Technology, University of M'sila, 28000 M'sila, Algeria

[7] Laboratory of Physics of Experimental Techniques and Their Applications (LPTEAM), University of Medea, Médéa, Algeria

[8] Department of Physics and Astronomy, College of Science, King Saud University, P.O. Box 2455, Riyadh 11451, Saudi Arabia

Published online: 27 September 2023

1 Introduction

The contemporary industry is making efforts to move away from hydrocarbons to eco-friendly technologies that utilize the properties of solids. These materials should be easy to process, recoverable, have a long lifespan, high efficiency, and be easily controlled by technological software algorithms integrated into microelectronic circuits. Microelectronic circuits are made of various types of semiconductors with different characteristics in terms of their energy gap value, stability, and sensitivity to light, temperature, pressure, and magnetic fields. Numerous materials have been investigated for use as semiconductors, with Heusler alloys being the most notable. Heusler alloys exist in various forms, including half, full, quaternary, and double, and in different magnetic states, such as ferromagnetic, anti-ferromagnetic, or non-magnetic. This is due to their half-metallicity in non-magnetic compounds or semiconducting behaviour in many compounds. Many theoretical [1–11] and experimental [12–19] studies on quaternary (QH), half (HH) and full (FH) Heusler compounds have demonstrated their eligibility for use in various technological applications, such as sensors, actuators, energy converters, magnetic shape-memory [20], thermoelectric generators [21–23], and magnetic cooling devices [24]. However, the high thermal expansion of these compounds has limited their use mainly to microelectronic circuits. It is relevant to point out that the relatively high cost associated with the specific chemical elements employed in Heusler alloys constitutes a major obstacle to their commercial proliferation. Therefore, recent scientific research has been primarily directed towards eliminating or reducing these high-cost constituents in Heusler alloys, without simultaneously compromising their effective attributes. For example, recent contributions by Shuo et al. [25] and Chauhan et al. [26] gave auspicious results regarding the advancement of economically viable Heusler alloys. These efforts provide compelling evidence that achieving high ZT (Factor of Merit) values in Heusler alloys is plausible without the use of exorbitantly expensive constituents, thus generating considerable cost savings. This marks a major advancement in the field of thermoelectrics, given its potential to lead to increased availability and accessibility of these materials. The study by Shuo et al. [25] demonstrated the possibility of achieving proportionate ZT values by reducing the concentration of the preeminent expensive component, hafnium (Hf), by one-third in the compound $Hf_xZr_{1-x}NiSn_{0.99}Sb_{0.01}$. This corresponds to an overall cost reduction of 50% in terms of material expenditure. Similarly, Chauhan et al. [26] corroborated this result by empirically studying the ramifications of the decrease in Hf concentration in the compound $Zr_{1-x}Hf_xNiSn$ on the thermoelectric power factor (PF), which clearly demonstrated an improvement. Nevertheless, it is imperative to emphasize that further scientific research is essential to optimize the attributes of Heusler alloys devoid of expensive chemical elements.

Ongoing research and studies on Heusler alloys have led to the emergence of a new Heusler materials type of double unit cell by mixing two-unit cells of half-Heusler alloys (XYZ) formed by two common chemical elements (X, Y or Z). This new type of double unit cell, known as double half-Heusler (DHH) that are characterized by the new chemical formula: $X'X''Y_2Z_2$, $X_2Y'Y''Z_2$, and $X_2Y_2Z'Z''$, has a distinct set of properties. Additionally, the unit cell can be tripled or quadrupled to form other types of Heusler alloys in triple or quadruple forms. Anand et al. [27] conducted pioneering research on double half-Heusler alloys and found that 315 of these alloys exhibit good thermodynamic stability with low lattice thermal conductivity. Furthermore, Slamani's research on $TiZrCo_2Bi_2$, $TiHfCo_2Bi_2$, and $ZrHfCo_2Bi_2$ DDH alloys [28] revealed that they are semiconductors with indirect band gaps in the range of 0.906 to 1.005 eV, satisfy the Born–Huang stability criteria, and are anisotropic, brittle, and ionic materials. These alloys also possess remarkable thermoelectric powers. Berarma et al. [29] studied the double half-Heusler alloys $Ta_2FeNiSn_2$ and $Nb_2FeNiSn_2$ and found that they exhibit large absorption coefficients in the UV spectrum and are classified as non-transparent materials. In another study, estimating the effective masses of electrons and holes in $LuXCo_2Sb_2$ (X = V, Nb and Ta) semiconductors showed that electrons are lighter and faster than holes, and exhibit anisotropic optical properties with strong absorption of incident electromagnetic radiation in a wide energy range [30].

The purpose of this research is to provide a comprehensive understanding of the fundamental physical properties of the double half-Heusler alloys $LuXNi_2Sn_2$ (X = V, Nb and Ta), which could have eventual potential applications in various fields including optoelectronics and thermoelectric energy conversion. Due to the lack of information regarding their physical properties, an investigation was conducted using state-of-the-art ab initio techniques to explore the structural stability, thermodynamic, optoelectronic, and thermoelectric properties of these materials. Moreover, the study aims to investigate the effect of spin-orbit interaction on these fundamental physical properties, since this interaction has a critical impact on the electronic structure and related properties of materials. The full-potential linearized augmented plane wave (FP-LAPW) method was utilized within the density functional theory framework to conduct the investigation. We hope that the results of this research will contribute significantly to the understanding of the fundamental physical properties of the considered materials.

Table 1 The calculated ground state lattice parameters (a, b, and c, in Å), and bulk modulus (B, in GPa) using full relativistic (FR) calculations and scalar relativistic (SR) calculations for the $LuXNi_2Sn_2$ (X = V, Nb, Ta) double half-Heusler materials

Compound	FR Calculations				SR Calculations			
	a b c B	*b*	*c*	*B*	*a b c B*	*b*	*c*	*B*
$LuVNi_2Sn_2$	4.2318	8.4471	6.0333	125.03	4.2304	8.4442	6.0313	122.60
$LuNbNi_2Sn_2$	4.2751	8.6060	6.0768	131.38	4.2737	8.6033	6.0749	130.63
$LuTaNi_2Sn_2$	4.2817	8.6018	6.0852	135.68	4.2754	8.5977	6.0741	134.93

2 Computational Methodology

The structural stability, electronic and optical properties of $LuXNi_2Sn_2$ (X = V, Nb, and Ta) double half-Heusler alloys were studied using the Full-Potential Linearized Augmented Plane Wave (FP-LAPW) method implemented in the WIEN2k code [31]. In order to estimate the exchange-correlation interaction for different calculations, two different methods were used. The Generalized Gradient Approximation PBEsol functional [32] was used for calculating the structural properties, while the modified Becke–Johnson potential (mBJ) [33] was used for calculating the band structure, total and partial densities, and the linear optical coefficients. In the framework of the FP-LAPW method, to solve the Kohn-Sham equation, the unit cell was divided into non-overlapping spheres, known as Muffin-tin spheres, which surround the atomic positions, and an interstitial residual space. The Muffin-tin spheres contain core electrons that were described by spherical harmonic functions with a maximum angular momentum l_{max} of up to 10, while the valence electrons in the interstitial area were described by plane waves with a cut-off parameter $R_{MT}^{min}K_{max} = 9$, where R_{MT}^{min} is the smallest muffin-tin radius and K_{max} is the magnitude of the largest k-vector. To optimize the structural properties, 80 special k-points were used for Brillouin zone (BZ) integration, and 216 special k-points were used for electronic, optical, and thermoelectric properties. The convergence criterion for the self-consistent calculations was set to be 10^{-4} Ry for all computation processes.

The effect of temperature and pressure on the thermal properties was evaluated using the quasi-harmonic Debye–Slater model integrated in the GIBBS2 code [34, 35] in combination with the FP-LAPW method.

The dependence of thermoelectric properties on the concentration of holes and electrons at fixed temperatures was investigated using the semi-classical Boltzmann transport theory as implemented in the BoltzTraP2 software [36] in combination with the FP-LAPW approach.

The complex dielectric function $\varepsilon(\omega)$; $\varepsilon(\omega) = \varepsilon_1(\omega) + i\varepsilon_2(\omega)$ [37], describes the linear optical responses of matter to incident electromagnetic radiation. It consists of two components: the real part ($\varepsilon_1(\omega)$) and the imaginary part ($\varepsilon_2(\omega)$). The real part ($\varepsilon_1(\omega)$) represents the dispersion of the medium, while the imaginary part ($\varepsilon_2(\omega)$) describes the absorption of the electromagnetic radiation as it passes through the medium. To calculate the spectrum of $\varepsilon_2(\omega)$, the electric dipole operator matrix elements between occupied and unoccupied wave functions are summed over the Brillouin zone, taking into account the selection rules [38]. This calculation provides insights into the absorption properties of the material. The spectrum of $\varepsilon_1(\omega)$, on the other hand, is obtained from the spectrum of $\varepsilon_2(\omega)$ using the

Table 2 The calculated ground state fractional atomic position coordinates using full relativistic (FR) calculations and scalar relativistic (SR) calculations for the $LuXNi_2Sn_2$ (X = V, Nb, Ta) double half-Heusler materials

Compound	Atom	FR Calculations			SR Calculations		
		x	*y*	*z*	*x*	*y*	*z*
$LuVNi_2Sn_2$	Lu	0.00	0.12195	0.49933	0.00000	0.12195	0.49933
	V	0.00	0.62329	0.62329	0.00000	0.62329	0.51476
	Ni(1)	0.50	0.15152	0.23490	0.50000	0.15152	0.23490
	Ni(2)	0.50	0.60951	0.26715	0.50000	0.60951	0.26715
	Sn(1)	0.50	0.38323	0.52400	0.50000	0.38323	0.52400
	Sn(2)	0.50	0.86149	0.49555	0.50000	0.86149	0.49555
$LuNbNi_2Sn_2$	Lu	0.00	0.12258	0.50081	0.00000	0.12265	0.50089
	Nb	0.00	0.62408	0.48883	0.00000	0.62408	0.48885
	Ni(1)	0.50	0.14348	0.76138	0.50000	0.14348	0.76138
	Ni(2)	0.50	0.61318	0.73291	0.50000	0.61319	0.73289
	Sn(1)	0.50	0.37839	0.48402	0.50000	0.37840	0.48403
	Sn(2)	0.50	0.86891	0.50439	0.50000	0.86890	0.50441
$LuTaNi_2Sn_2$	Lu	0.00	0.11546	0.48684	0.00000	0.12210	0.49832
	Ta	0.00	0.61816	0.48437	0.00000	0.62395	0.50943
	Ni(1)	0.50	0.14712	0.22434	0.50000	0.14345	0.23811
	Ni(2)	0.50	0.61110	0.25233	0.50000	0.61202	0.26678
	Sn(1)	0.50	0.37449	0.49866	0.50000	0.37770	0.51503
	Sn(2)	0.50	0.86419	0.48553	0.50000	0.86850	0.49511

Kramers-Kronig relationship [37]. This relationship allows for the determination of the dispersion properties of the material based on its absorption spectrum. The spectra of other linear optical parameters, such as the refractive index, extinction coefficient, reflectivity, and absorption coefficient, can be derived from the spectra of $\varepsilon_1(\omega)$ and $\varepsilon_2(\omega)$ using well-known relationships [38]. These relationships enable the extraction of additional optical properties based on the calculated spectra of $\varepsilon_1(\omega)$ and $\varepsilon_2(\omega)$, providing a comprehensive understanding of the material's optical behaviour.

3 Results and Discussion

3.1 Stability, Structural Parameters and Thermodynamic Properties

$LuXNi_2Sn_2$ (X = V, Nb and Ta) double half-Heusler materials possess an orthorhombic crystal structure belonging to the space group $Pmn2_1$ (#31) [39, 40]. The optimized lattice parameters (*a*, *b*, *c*), and atomic position coordinates are given in Tables 1 and 2. The equilibrium atomic position coordinates were obtained by relaxing the atomic positions using the Brayden scheme force minimization [41]. For the purpose of ascertaining the structural parameters in the ground state (*a*, *b*, and *c*) and the compressibility modulus (B), the total energies (E_{Tot}) of the unit cell were computed across a spectrum of predetermined volumes (V) of the unit cell. Subsequently, the acquired $E_{Tot} - V$ dataset was subjected to fitting procedures utilizing Murnaghan's equation of state (EOS) [42]. It should be underscored that the computations pertaining to the equilibrium structural parameters were conducted employing two distinct approaches: one that accounts for the spin-orbit coupling (SOC), denoted as "full relativistic calculations (FR)," and another that omits SOC, denoted as "scalar relativistic calculations (SR)". Upon comparing the values of the structure parameters obtained with and without including SOC for the investigated materials, it can be observed that the effect of SOC is quite negligible for the $LuVNi_2Sn_2$ compound. However, as the weight of the X (X = V, Na, Ta) atom increases, the impact of SOC becomes more significant.

To check the thermodynamic stability of the considered double half-Heusler materials, the formation enthalpy (ΔH_{for}), a measure of the energy released or consumed when one mole of a substance is created under standard conditions from its pure elements, was calculated through the known relationship [30]:

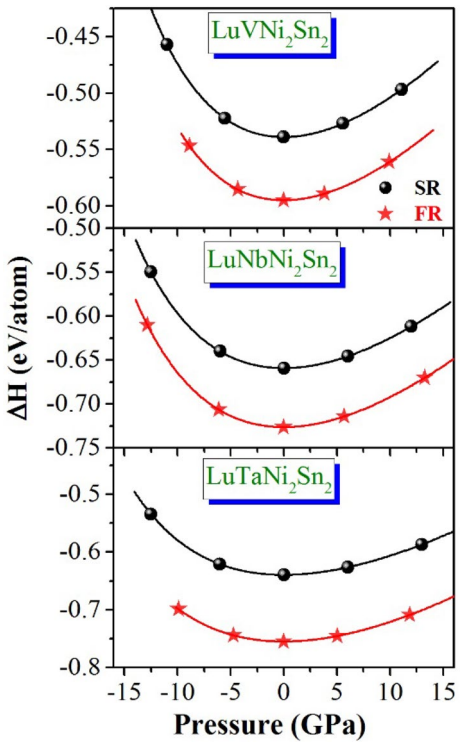

Fig. 1 The pressure-dependent variations in formation enthalpy for $LuXNi_2Sn_2$ (X = V, Nb and Ta). These calculations were conducted both with and without the incorporation of spin-orbit coupling effects. *FR* The outcomes of full relativistic calculations, *SR* The outcomes of scalar relativistic calculations

In this context, $E_{tot}^{LuXNi_2Sn_2}$ is the total energy of $LuXNi_2Sn_2$ compound, E_{solid}^{Lu} ; E_{solid}^{Ni};E_{solid}^{Sn} ; E_{solid}^{X} are the energies of the constituent elements, namely Lu, Ni, Sn and X atoms, respectively, in their solid state, and n_{Lu}; n_{Ni}; n_{Sn}; n_X are the number of the Lu, Ni, Sn and X atoms, respectively, in the unit cell. It is found that the enthalpies of formation of the three considered double half-Heusler materials are negative ($\Delta H_{form}^{LuVNi_2Sn_2} = -0.595\,eV$; $\Delta H_{form}^{LuNbNi_2Sn_2} = -0.727\,eV$; $\Delta H_{form}^{LuTaNi_2Sn_2} = -0.755\,eV$). These results highlight the thermodynamic stability of $LuXNi_2Sn_2$ (X = V, Nb and Ta) double half-Heusler alloys. Additionally, pressure dependence of the formation enthalpy for $LuXNi_2Sn_2$ (X = V, Nb and Ta) double half-Heusler alloys were calculated and depicted in Fig. 1. It is evident from Fig. 1 that the three studied compounds are thermodynamically stable; the

$$\Delta H_{for}\left(\frac{eV}{atom}\right) = \frac{E_{tot}^{LuXNi_2Sn_2} - \left(n_{Lu}E_{solid}^{Lu} + n_X E_{solid}^{X} + n_{Ni}E_{solid}^{Ni} + n_{Sn}E_{solid}^{Sn}\right)}{n_{Lu} + n_X + n_{Co} + n_{Sb}}$$

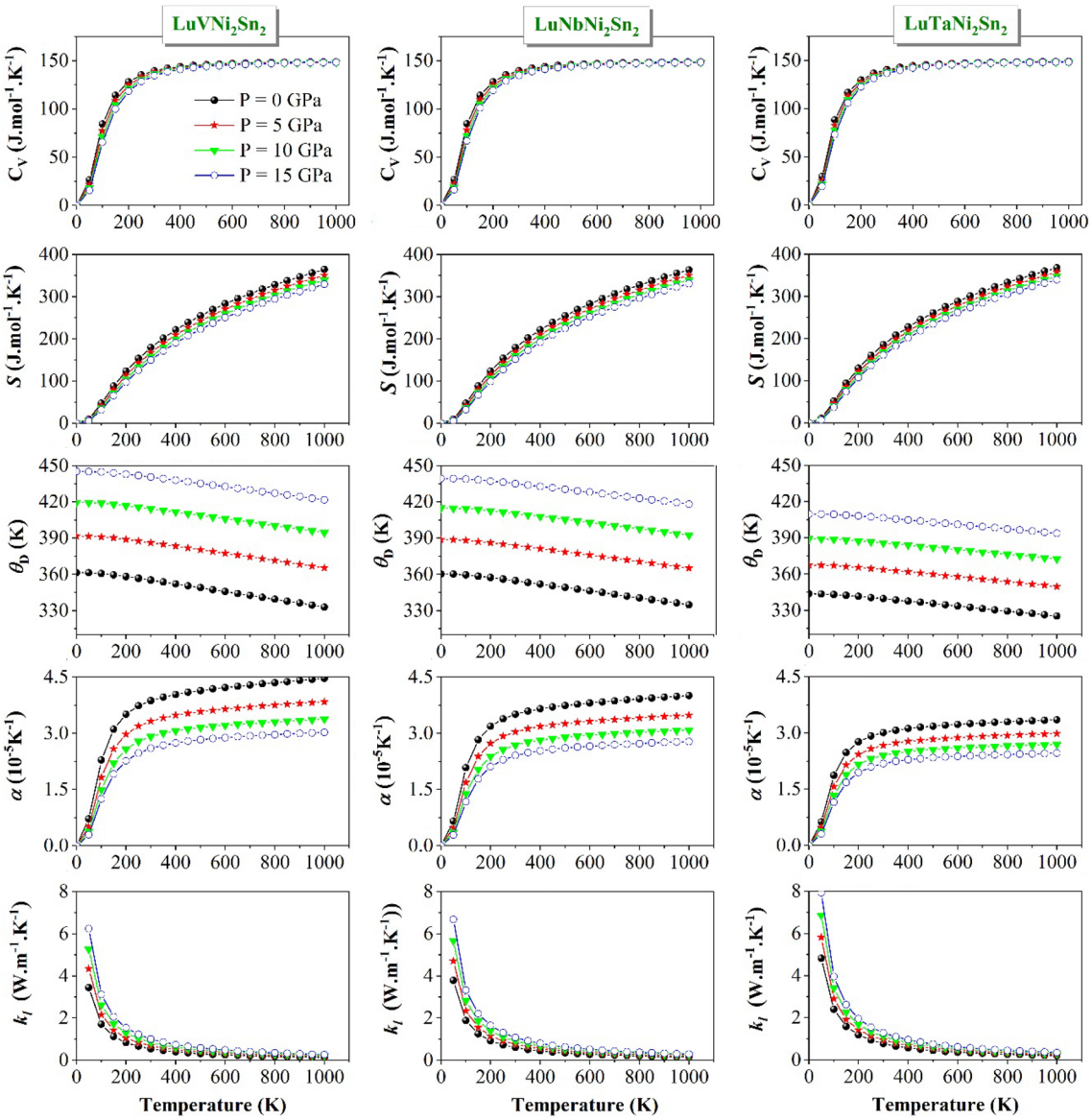

Fig. 2 Temperature and pressure dependencies of the isochoric heat capacity (C_V), lattice thermal conductivity (k_l), entropy (S), thermal expansion (α), and Debye temperature (θ_D) of LuXNi$_2$Sn$_2$ (X = V, Nb and Ta) double half Heusler alloys

formation enthalpy is negative even under the imposition of pressures in excess of 15 GPa.

The primary requisite for Heusler alloys resides in their adherence to the principle of balanced valence, as encapsulated by the valence rule ($N_V = 0$) [27]. A noteworthy illustration of this principle is embodied by the double half-Heusler alloys LuXNi$_2$Sn$_2$, where X can represent vanadium (V), niobium (Nb), or tantalum (Ta). These alloys unequivocally validate the concept of valence equilibrium (quantified as net valence equilibrium, $N_V = 0$): $N_V(LuXNi_2Sn_2) = 3[Lu^{+3}; s^0d^0] + 5[X^{+5}; s^0d^0] + 2 \times 0[Ni^0; s^0d^{10}] + 2 \times (-4)(Sn^{-4}; s^2p^6) = 0$. Strikingly, this is in stark contrast to their half-Heusler precursors, specifically LuNiSn and XNiSn (where X = V, Nb, or Ta), which manifestly fail to satisfy this criterion. More specifically, for $N_V(LuNiSn) = \times\ 3[Lu^{+3}; s^0d^0] + 1 \times 0[Ni^0; s^0d^{10}] + 1 \times (-4)(Sn^{-4}; s^2p^6) = -1 \neq 0$, and $N_V(XNiSn) = 1 \times 5[X^{+5}; s^0d^0] + 1 \times 0[Ni^0; s^0d^{10}] + 1 \times (-4)[Sn^{-4}; s^2p^6] = 1 \neq 0$.

3.2 Thermodynamic Properties

We have investigated the thermodynamic properties, including thermal expansion coefficient (α), Debye temperature (θ_D), entropy (S), heat capacity at constant volume (C_V), and lattice thermal conductivity (K_l), for LuVNi$_2$Sn$_2$, LuNbNi$_2$Sn$_2$, and LuTaNi$_2$Sn$_2$ materials in a temperature

range of 0 to 1000 K at fixed pressures of 0, 5, 10, and 15 GPa.

The thermal expansion coefficient (α) is a physical property that describes the response of a crystal lattice vibration to changes in volume resulting from changes in temperature. This property is an essential parameter in the study of materials science and engineering and plays a crucial role in the development of new materials with specific thermal properties. In this study, the variation of the thermal expansion coefficient with temperature at fixed pressure values is shown in Fig. 2 for $LuXNi_2Sn_2$ (X = V, Nb, Ta) Heusler alloys. The results indicate that the thermal expansion coefficient increases rapidly with temperature up to 300 K, beyond which it increases more gradually with temperature. At a constant temperature, the thermal expansion coefficient decreases as pressure increases. This behaviour is consistent with the general trend observed in materials, where thermal expansion coefficients tend to decrease as pressure increases. At a temperature of 300 K and zero pressure, the volume thermal expansion coefficient is 2×10^{-5} K^{-1}.

Figure 2 shows the Debye temperature (θ_D) as a function of temperature at fixed pressure values (0, 5, 10, and 15 GPa) for the considered Heusler compounds. The results indicate that the effect of temperature on θ_D is opposite to that of pressure. Specifically, at a given temperature, θ_D increases with increasing pressure, while it decreases with increasing temperature at a given pressure. The behaviour of θ_D over the temperature range from 0 to 100 K remains unchanged, after which it decreases with increasing temperature at a fixed pressure. These findings suggest that the thermal vibration frequency of atoms in Heusler compounds varies with changes in temperature and pressure. Using the quasi-harmonic Debye–Slater model, we calculated the values of θ_D at zero temperature and zero pressure to be 362 K, 360 K, and 350 K for $LuVNi_2Sn_2$, $LuNbNi_2Sn_2$, and $LuTaNi_2Sn_2$ Heusler alloys, respectively.

Variations of the heat capacities at constant volume (C_V) with temperature at fixed pressures for $LuXNi_2Sn_2$ materials, where X = V, Nb, Ta, have been calculated, and presented in Fig. 2. The figure shows that C_V of $LuXNi_2Sn_2$ compound increases rapidly with increasing temperature for temperatures less than 300 K. This is because the increase in temperature induces a rapid activation of new vibration modes, which leads to a rapid increase in the number of ways that the atoms in the compound can vibrate. The heat capacity C_V then increases more moderately to converge to the Dulong–Petit limit at high temperatures [43]. The Dulong–Petit limit is a constant value of C_V equal to $3nN_Ak_B$, where n is the number of atoms in the unit cell (it is 6 in $LuXNi_2Sn_2$), N_A represents Avogadro's number, and k_B represents Boltzmann's constant. The Dulong–Petit limit in the considered compounds is equal to = 150 J mol^{-1} K^{-1}. The tendency of C_V can be attributed to the fact that the constituent atoms of $LuXNi_2Sn_2$ can vibrate only in limited number and at high temperature, all possible vibrational modes are activated, and thus C_V reaches its limit value, known as Dulong–Small limit.

The entropy (S) of $LuXNi_2Sn_2$ materials, where X = V, Nb, Ta, was calculated at fixed pressures of 0, 5, 10 and 15 GPa, and the results are shown in Fig. 2. The results suggest that the entropy (S) of these compounds is zero at 0 K and increases rapidly with increasing temperature. Also, Fig. 2 shows that the entropy (S) decreases with increasing pressure at fixed temperature. These results are in line with our expectations, because the entropy at the microscopic level expresses the disorder of the system (chaos and randomness), that is to say the number of configurations that a physical system can take ($S = k_B ln(\Omega)$, where Ω denotes the number of possible configurations while k_B represents the Boltzmann constant) [44]. Consequently, the increasing pressure reduces these states and restricts the freedom

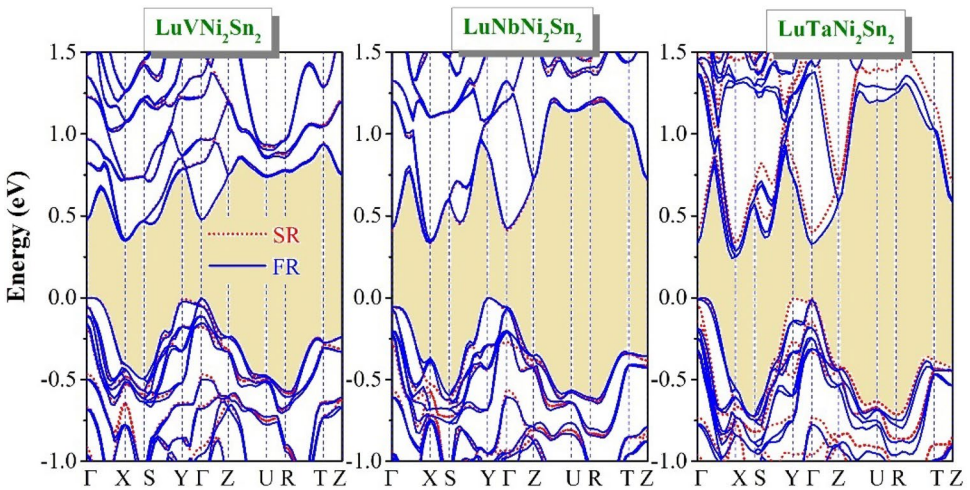

Fig. 3 The calculated energy band dispersions along the line of high symmetry in the Brillouin zone for the compounds $LuVNi_2Sn_2$, $LuNbNi_2Sn_2$, and $LuTaNi_2Sn_2$. The red curves correspond to the results obtained using the TB-mBJ-SR approach, while the blue curves correspond to the results obtained using the TB-mBJ-FR approach

Table 3 The predicted energy bandgaps (E_g, in eV) using the Tb-mBJ potential both without including SOC (scalar relativistic calculations; SR calc.) and with including SOC (full relativistic calculations; FR calc.), as well as the effective masses of holes and electrons ($m_h^*$and m_e^*, in m_0 unit) at the VBM located at the Y point in BZ and the CBM located at X point in BZ, respectively, towards three different directions in BZ that correspond to the crystal directions [100], [010] and [001] that are deduced from band structures calculated using the Tb-mBJ potential with including SOC (full relativistic calculations; FR calc.) for the $LuVNi_2Sn_2$, $LuNbNi_2Sn_2$ and $LuTaNi_2Sn_2$ materials

	$LuVNi_2Sn_2$		$LuNbNi_2Sn_2$		$LuTaNi_2Sn_2$	
	SR calc.	FR calc.	SR cal.	FR calc.	SR calc.	FR calc.
E_g(eV)	0.351	0.345	0.331	0.336	0.334	0.241

Material	m_e^*			m_h^*		
	X–S	X–T	X–U	Y–T	Y–S	Y–T
$LuVNi_2Sn_2$	0.491	0.182	0.173	0.162	0.203	0.450
$LuNbNi_2Sn_2$	0.245	0.165	0.108	0.143	0.146	0.372
$LuTaNi_2Sn_2$	0.302	0.110	0.110	0.109	0.192	0.227

of vibration of the atoms, thus decreasing the number of disorder states.

The lattice thermal conductivity (κ_l) is a critical thermodynamic property that characterizes the ability of materials to transfer heat when there is a temperature difference between their two ends. It is an essential factor in understanding the thermal behavior of materials, particularly in applications that involve heat transfer. The lattice thermal conductivity of the crystal lattice of the considered materials has been numerically estimated by employing the Slack model formula [45], which is a widely used model for calculating the lattice thermal conductivity of materials. The Slack formula to estimate κ_l is given by the following formula [45]: $\kappa_l = \frac{A\theta_D{}^3 V^{1/3} m}{\gamma^2 n^{2/3} T}$

In this context, $A = \frac{2.4310^{-8}}{1-\frac{0.514}{\gamma}+\frac{0.228}{\gamma^2}}$ is a physical constant, and θ_D, γ, V, n and m denote the Debye temperature, Grüneisen parameter, the volume per atom, the number of atoms in the primitive unit cell and the atomic mass, respectively. The κ_l variation as a function of temperature at some fixed pressures is depicted in Fig. 2 for $LuXNi_2Sn_2$ (X = V, Nb, Ta) Heusler compounds. It can be observed that κ_l decreases (increases) with increasing temperature (pressure), and they are fitted well with the $\kappa_l \sim 1/T$ relationship.

3.3 Electronic Properties

3.3.1 Energy Band Dispersions

The energy dispersions of $LuVNi_2Sn_2$, $LuNbNi_2Sn_2$, and $LuTaNi_2Sn_2$ compounds were computed for specific high-symmetry directions; namely $\Gamma \rightarrow X \rightarrow S \rightarrow Y \rightarrow \Gamma \rightarrow Z \rightarrow U \rightarrow R \rightarrow T \rightarrow Z$, within the Brillouin zone. The calculations were conducted using two approaches: one considering the interaction between the spin and orbital angular momentum of electrons, known as spin-orbit coupling (SOC), which represents a full relativistic (FR) calculation, and the other without taking spin-orbit coupling into account, known as a scalar relativistic (SR) calculation. In the context provided, the term "FR" is used to denote the inclusion of the spin-orbit interaction in the calculations, whereas the term "SR" indicates the absence of spin-orbit coupling. The results obtained from these calculations are depicted in Fig. 3. The band structures of the three investigated compounds exhibit similar characteristics. The SR calculations yield that the three considered materials possess indirect band gaps, with $LuVNi_2Sn_2$ and $LuTaNi_2Sn_2$ having gaps between Γ and X points and $LuNbNi_2Sn_2$ having a gap between Y and X points, while the FR calculations show that the three considered materials have indirect band gaps of the Y–X type. These band gaps have relatively small values, which do not exceed 0.4 eV. Table 3 summarizes the calculated values of the energy band

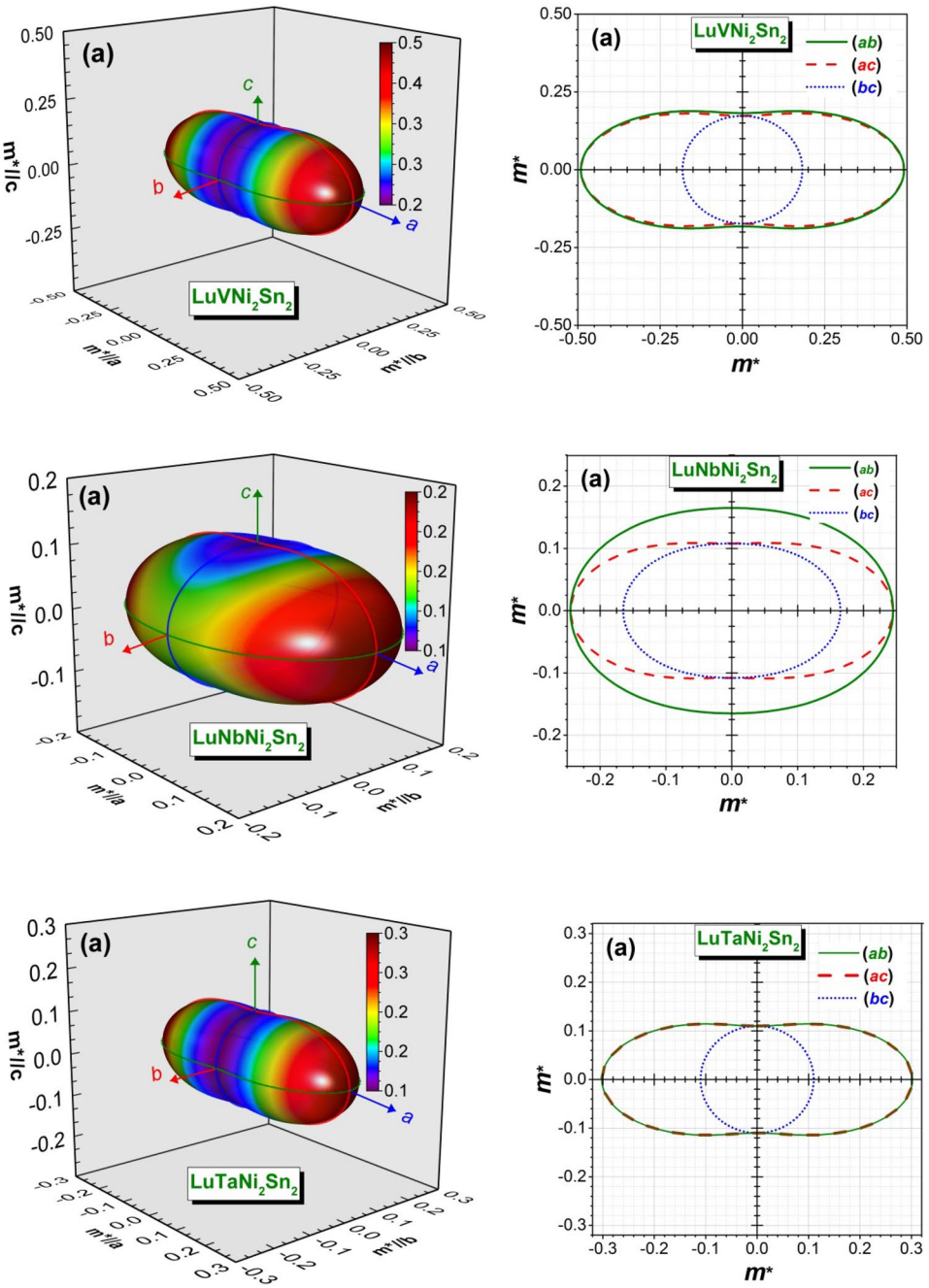

Fig. 4 3D-representations of the crystal direction dependent effective masses of electrons at X-point and their cross-sections in the (001); (ab), (010); (ac) and (100); (bc) crystalline planes for the $LuXNi_2Sn_2$ (where X can be V, Nb, or Ta) materials

gaps (E_g) of the explored materials obtained using two different computational methods, namely the TB-mBJ-SR and TB-mBJ-FR approaches. It is worth noting that the energy band dispersions obtained from both TB-mBJ-SR and TB-mBJ-FR calculations are presented in the same figure to facilitate comparison. Based on the information provided in Fig. 3 and Table 3, the following conclusions can be drawn.

(i) When considering the spin-orbit coupling interaction, the initially degenerate conduction levels split and shift toward the Fermi level. This results in a slight reduction in the band gap. Particularly, this reduction is more pronounced in the conduction region between the Γ and X points for the $LuTaNi_2Sn_2$ compound. The shift values of the conduction bands along the Γ and X directions are approximately 0.07 and 0.09 eV, respectively.

(ii) The energy band-gap values of $LuXNi_2Sn_2$ double half-Heusler alloys exhibit a slight decrease when the V atom is substituted with the Nb atom, and a significant decrease when substituted with the Ta atom. This indicates that the introduction of Nb or Ta atoms

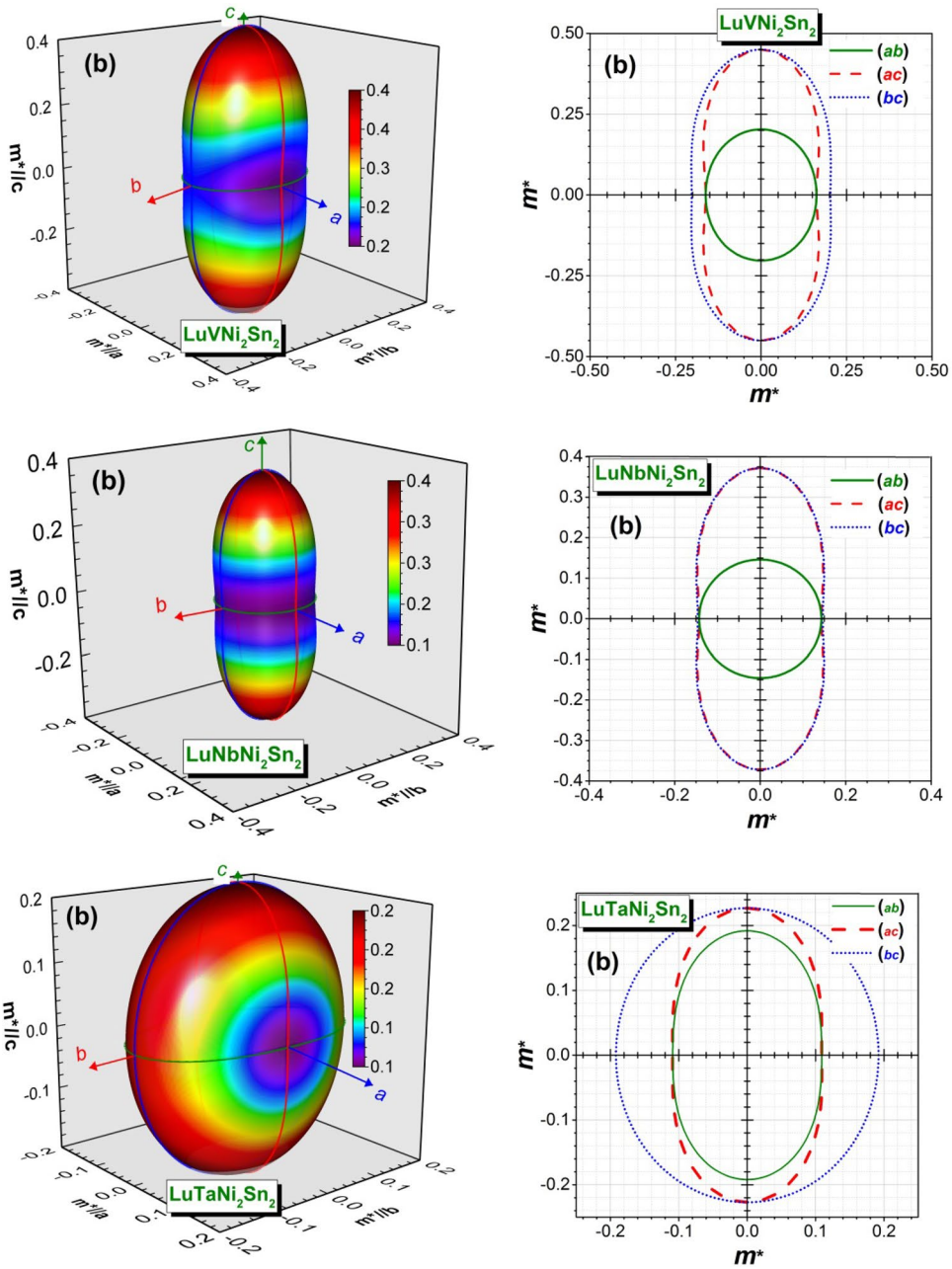

Fig. 5 3D-representations of the crystal direction dependent effective masses of holes at Y-point and their cross-sections in the (001); (ab), (010); (ac) and (100); (bc) crystalline planes for the $LuXNi_2Sn_2$ (where X can be V, Nb, or Ta) materials

into the compound affects the energy band structure, leading to alterations in the electronic properties.

3.3.2 Charge Carrier Effective Masses

To determine the effective masses of charge carriers in the studied materials, we performed numerical estimates normalized to the free electron mass (m_0) for both holes and electrons. These estimates were obtained by fitting the energy band dispersion E(k) in the vicinity of the Valence Band Maximum (VBM) and the Conduction Band Minimum (CBM) to a parabolic function, $E(k) = Ak^2$. The effective mass (m*) for holes and electrons, denoted as m_h^* and m_e^*, respectively, can then be deduced using the following relationship: $\frac{1}{m*} = \frac{m_0}{\hbar^2}\frac{\partial^2 E(k)}{\partial k^2}\Big|_{k=k_0}$, where $\hbar$ is the reduced Planck's constant, $\frac{\partial^2 E(k)}{\partial k^2}$ represents the second derivative of the energy dispersion with respect to the wave vector k, and k_0 is an extreme point in the Brillouin zone. The calculated effective masses for holes and electrons; m_h^* and m_e^*, respectively, at the VBM and CBM are presented in Table 3. These extreme points are located at the Y and X points, and the effective masses were calculated with

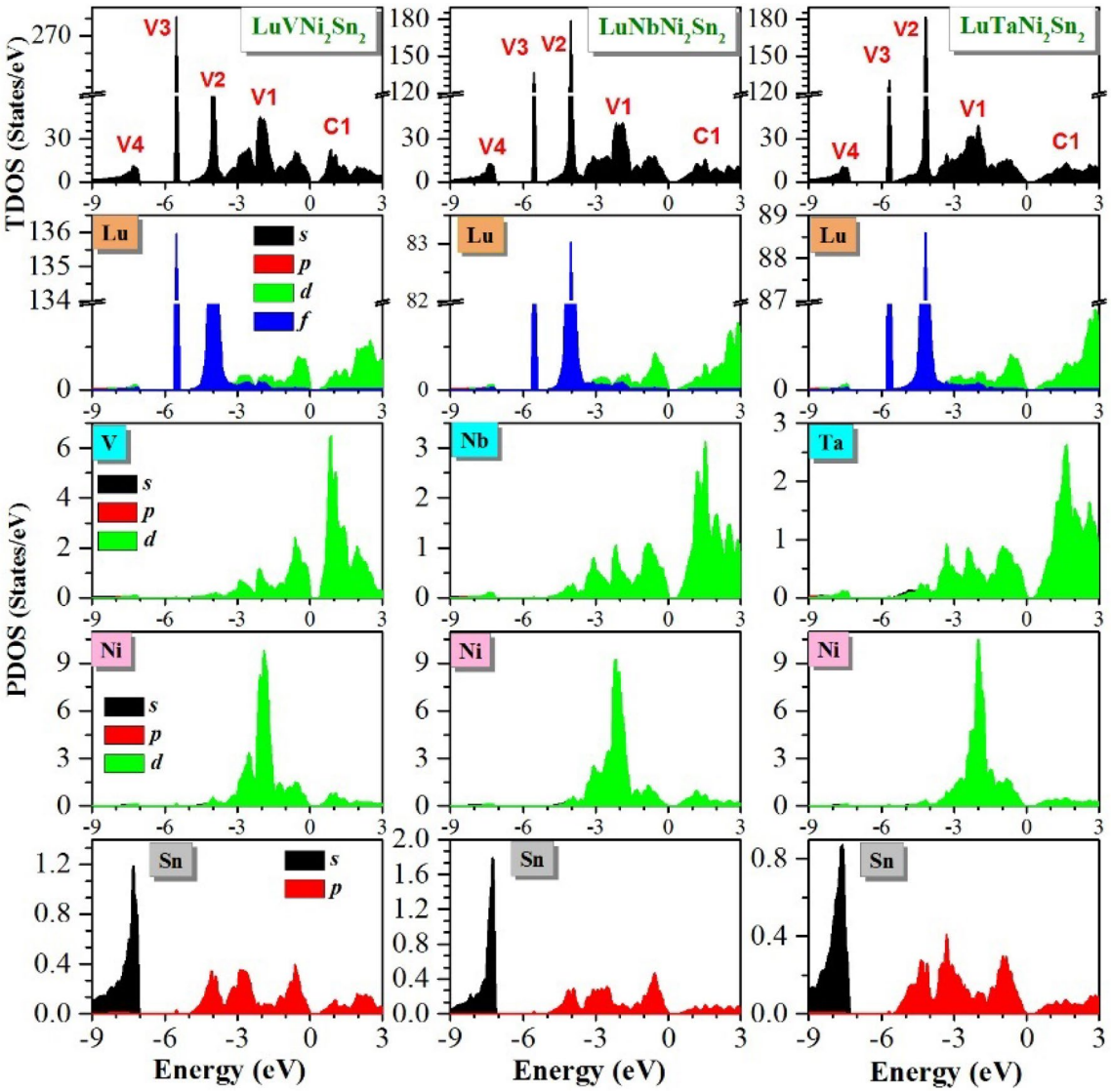

Fig. 6 The calculated diagrams of the total and partial densities of states (TDOS and PDOS) for the $LuVNi_2Sn_2$, $LuNbNi_2Sn_2$ and $LuTaNi_2Sn_2$ compounds using the TB-mBJ potential with including the spin-orbit coupling (SOC).

directions towards Γ, S, and T for holes, and towards S, Γ, and U for electrons in the Brillouin zone. Notably, the directions Y → Γ/X → S, Y → S/X → Γ, and Y → T/X → U in the Brillouin zone correspond to the [100], [010], and [001] crystalline directions, respectively. It is observed that the effective mass of holes is greater than that of electrons along the [010] and [010] directions. Conversely, the effective mass of electrons is greater than that of holes along the [100] direction. This indicates that the contribution of holes to the electrical current will be significantly larger than that of the same concentration of electrons along the [100] direction. Similarly, the contribution of electrons will be larger than that of the same concentration of holes along the [010] and [001] directions. The heaviest effective mass for electrons is observed along the [100] direction, while the heaviest effective mass for holes is along the [001] direction. It is known that charge carrier effective masses are inversely (directly) proportional to electrical conductivity (the Seebeck coefficient). Thus, the title compounds are expected to exhibit the smallest electrical conductivity but the highest Seebeck coefficient along the [001] direction for holes, and along the [001] direction for electrons.

The effective masses of holes and electrons in an arbitrary direction, infinitesimally close to the extreme points, in an orthorhombic system can be obtained using the following relationship [46]: $m^* = \frac{1}{\cos^2(\alpha)/m^*_{[100]} + \cos^2(\beta)/m^*_{[010]} + \cos^2(\gamma)/m^*_{[001]}}$, where α, β, and γ are the angles between the specific direction and the [100], [010], and [001] crystalline directions,

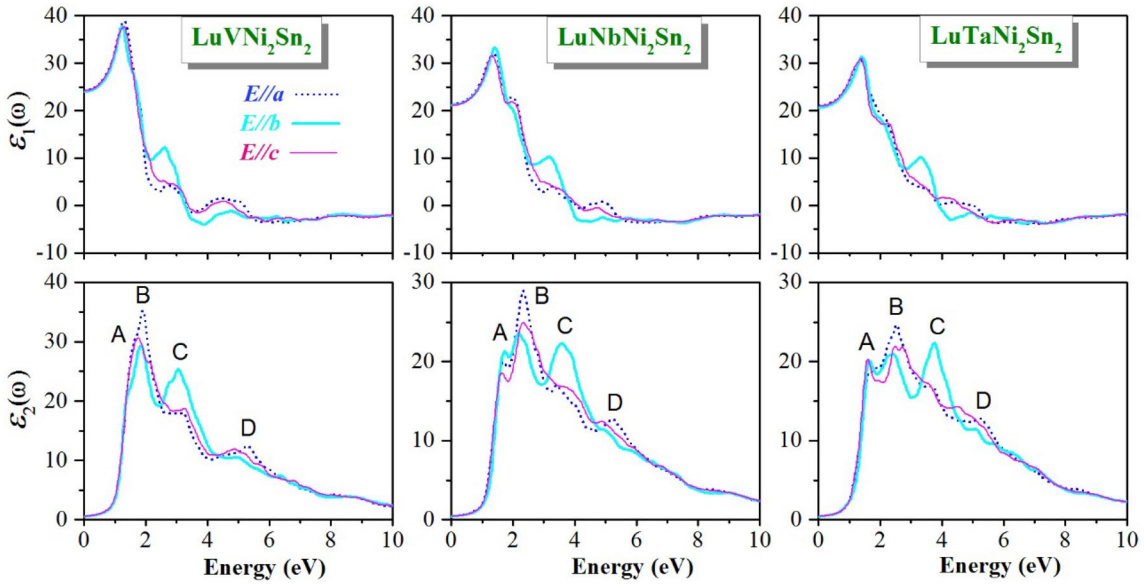

Fig. 7 The Calculated frequency-dependent imaginary part ($\varepsilon_2(\omega)$) and real part ($\varepsilon_1(\omega)$) of the complex dielectric function for the $LuVNi_2Sn_2$, $LuNbNi_2Sn_2$ and $LuTaNi_2Sn_2$ compounds using the TB-mBJ potential with including the spin-orbit coupling (SOC)

respectively. Figures 4 and 5 illustrate three-dimensional representations of the crystal direction dependencies of effective masses for holes and electrons at the Y and X points, respectively, as well as their two-dimensional representations in the (100), (010), and (001) crystalline planes. These representations clearly demonstrate that the charge carrier effective masses in the title compounds exhibit strong anisotropy. Consequently, transport parameters such as mobility and the Seebeck coefficient are also expected to exhibit significant anisotropy.

3.3.3 Density of States

Figure 6 illustrates the total and atomic-projected *l*-decomposed densities of states (TDOS and PDOS) for the compounds under investigation. The upper valence band group (V1 in Fig. 6) is formed by the hybridized Ni: 3*d* and X: n*d* orbitals, where X represents V (n = 3), Nb (n = 4), or Ta (n = 5). This group spans the energy range from approximately − 3.6 to 0 eV. The valence band group, designated as V2 in Fig. 6, which ranges from approximately − 4.9 to − 3.6 eV, is predominantly influenced by the Lu: 5*d* states, with a minor contribution from the Sn: 5*p* states. Another valence band group, labeled as V3 in Fig. 6, which centered around − 5.5 eV, is primarily attributed to the Lu: *f* states. The lowest energy valence band group, denoted as V4 in Fig. 6, which spans from approximately − 9 to − 7 eV, is originated from the Sn: *p* states. The conduction band bottom is also composed of states associated with the [LuX] blocks. Consequently, both the valence band maximum (VBM) and conduction band minimum (CBM) are entirely composed of the Lu: 5*d* and X: n*d* states from the [LuX] blocks.

3.4 Optical Properties

The optical properties of double half-Heusler compounds exhibit variations depending on their composition and crystal structure. Some compounds demonstrate significant absorption in the ultraviolet region, while others exhibit strong absorption in the visible region [29, 30]. These optical properties play a crucial role in applications such as photovoltaics, where efficient light absorption is necessary for effective energy conversion.

In this study, we conducted calculations to determine the optical properties of $LuXNi_2Sn_2$ (X = V, Nb, and Ta) compounds within an energy range of 0 to 20 eV. We focused on evaluating the dielectric function as a function of frequency, which allowed us to derive additional optical properties such as optical conductivity, refractive indices, absorption coefficient, and optical reflectivity. Figure 7 illustrates the spectra of the imaginary part of the optical dielectric function ($\varepsilon_2^{vv}(\omega)$; $v = x, y, z$) for incident electromagnetic waves with electric field vectors E parallel to the three principal crystalline axes, namely **E**||**a**, **E**||**b**, and **E**||**c**. Each spectrum of the materials under consideration exhibits four distinct structures labeled A, B, C, and D in Fig. 7. In the spectrum $\varepsilon_2^{vv}(\omega)$ of $LuVNi_2Sn_2$, the A and B peaks overlap, whereas in $LuNbNi_2Sn_2$ and $LuTaNi_2Sn_2$, these peaks are well distinguished. These peaks arise from direct electronic transitions occurring between occupied states in the valence band

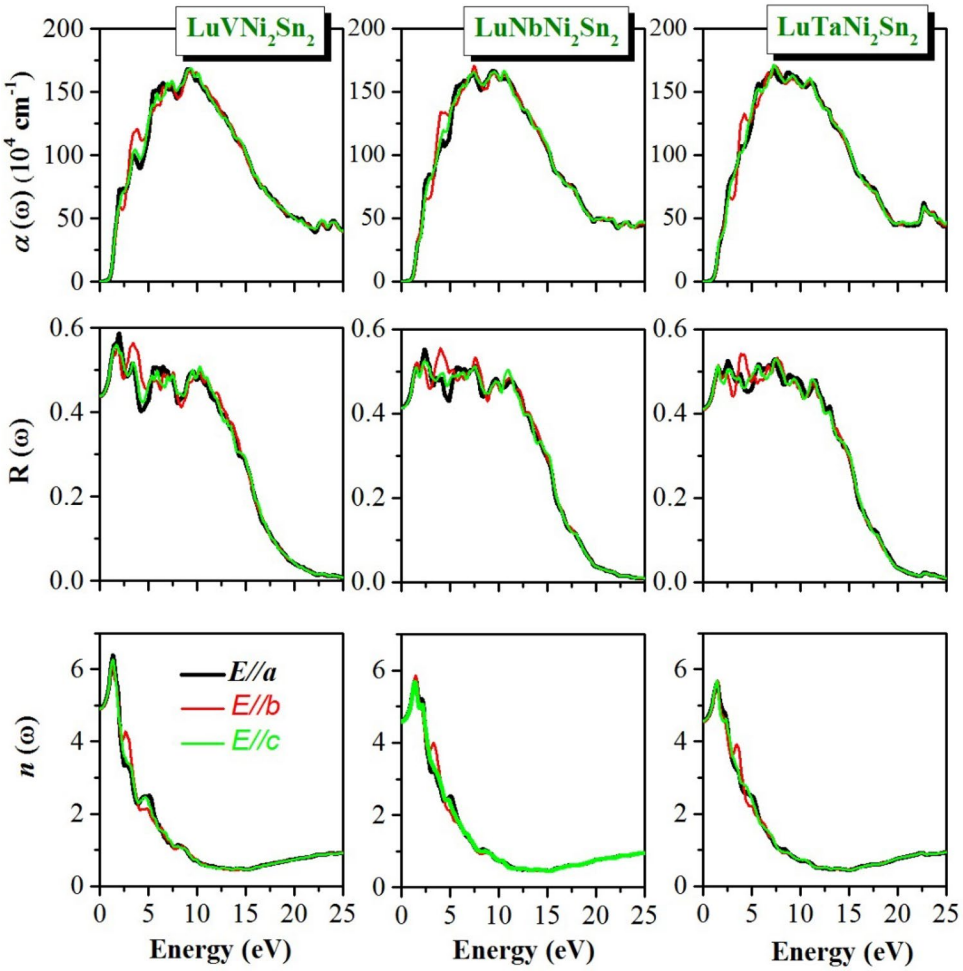

Fig. 8 The Calculated frequency-dependent absorption coefficient $\alpha(\omega)$, The Reflectivity $R(\omega)$, refractive index $n(\omega)$ for the $LuVNi_2Sn_2$, $LuNbNi_2Sn_2$ and $LuTaNi_2Sn_2$ compounds using the TB-mBJ potential with including the spin-orbit coupling (Full relativistic calculations)

and unoccupied states in the conduction band. Analysis of Fig. 7 reveals that the energy positions and magnitudes of the major peaks in the spectra of $\varepsilon_2^{vv}(\omega)$ ($v = x, y, z$) differ considerably within the energy range of 1 to 7 eV, while they appear almost superimposed in the remaining energy range. Furthermore, the magnitude of the structure corresponding to **E**||**b** is slightly larger than those corresponding to *E*||**a** and **E**||**c**. These observations indicate a distinct anisotropy in the imaginary part of the dielectric function ($\varepsilon_2(\omega)$) within the energy range of 1 to 7 eV, while it demonstrates nearly isotropic behavior in the remaining energy range for both studied compounds. An intriguing avenue for further investigation is to elucidate the nature of the optical transitions responsible for the observed structures in the spectrum. By referring to the partial density of states (PDOS) diagrams presented in Fig. 6, one can assign the observed structures A and B in the spectrum to electronic transitions from the valence sub-bands V1 and V2 to the conduction sub-band C1. These transitions involve the filled Ni-3*d* and X-n*d* states transitioning to the empty Lu-5*d* and X-n*d* states (where n = 3 for V, n = 4 for Nb, and n = 5 for Ta). Structure C can be attributed to the electronic transition from the V2 valence sub-band to the C1 conduction sub-band, involving the filled As-4*p* and Ga-4*p* states transitioning to the empty Sr/Ba-n*d* states (where n = 3 for Sr and n = 4 for Ba). Finally, structure D corresponds to the electronic transition from the V3 valence sub-band to the C1 conduction sub-band, where the filled As-4p and Ga-4p states transition to the empty Sr/Ba-nd states (where n = 3 for Sr and n = 4 for Ba).

Figure 7 also presents the spectra of the real part of the dielectric function ($\varepsilon_1(\omega)$) for the three crystal axes, namely $\varepsilon_1^{vv}(\omega)$ ($v = x, y, z$). Notably, these spectra exhibit clear anisotropy within the energy range of approximately 2 to 6 eV for all the compounds studied. Each curve of $\varepsilon_1^{vv}(\omega)$ ($v = x, y, z$) shows an increasing trend as the photon energy rises from its static value, reaching a maximum, and then gradually decreasing. The magnitudes of the $\varepsilon_1^{vv}(\omega)$ ($v = x, y, z$) spectra do not exhibit consistent differences. The maximum magnitude of $\varepsilon_1(\omega)$ is approximately 38.6 at around 1.26 eV in $LuVNi_2Sn_2$, 33.29 at around 1.39 eV in $LuNbNi_2Sn_2$, and 31.23 at around 1.43 eV in $LuTaNi_2Sn_2$. Furthermore, the calculated values of the electronic static dielectric constant for all three polarizations $\varepsilon_1^{vv}(\omega \to 0)$ ($v = x, y, z$) are identical. The value of $\varepsilon_1^{vv}(0)$ ($v = x, y, z$) is 23.8 in $LuVNi_2Sn_2$,

21.4 in $LuVNi_2Sn_2$, and 20.6 in $LuVNi_2Sn_2$. These values follow a decreasing trend according to the sequence: $LuVNi_2Sn_2 \rightarrow LuNbNi_2Sn_2 \rightarrow LuTaNi_2Sn_2$. This observation aligns with Penn's model [47], which proposes an inverse proportionality between $\varepsilon(0)$ and the bandgap value.

Certain optoelectronic devices, such as sunlight converters, rely on the absorption spectra of semiconductors for their functionality. The absorption coefficient, denoted as $\alpha(\omega)$, provides a measure of the energy absorbed per unit length of a medium when it is exposed to an electromagnetic wave of frequency ω. In this study, the frequency-dependent absorption coefficient curves were calculated for the specific compounds under investigation within an energy range up to 25 eV. The incident electromagnetic radiation was polarized parallel to the [100], [010], and [001] crystalline directions, denoted as $\alpha^{xx}(\omega)$, $\alpha^{yy}(\omega)$ and $\alpha^{zz}(\omega)$, respectively (see Fig. 8a). Each absorption $\alpha^{yy}(\omega)$ spectrum within the considered energy range exhibited a prominent absorption band spanning from the absorption threshold to 25 eV. It is worth noting that the $\alpha^{xx}(\omega)$, $\alpha^{yy}(\omega)$ and $\alpha^{zz}(\omega)$ curves initiate from the same absorption threshold and exhibit similar rapid growth rates, indicating an isotropic band edge. For the three compounds analyzed, $\alpha^{xx}(\omega)$, $\alpha^{yy}(\omega)$ and $\alpha^{zz}(\omega)$ display values higher than $\sim 169 \times 10^4$ cm^{-1} within an energy range approximately ranging from 5 to 11 eV. Moreover, the magnitude of the absorption coefficient surpasses 10^6 cm^{-1} over a significant energy span ranging from approximately 3 to 15 eV. Notably, for $LuVNi_2Sn_2$, $LuNbNi_2Sn_2$, and $LuTaNi_2Sn_2$, the absorption coefficient magnitude exceeded 5×10^5 cm^{-1} across a wide energy range spanning approximately from 1.6 to 20 eV, 2 to 19.5 eV, and 2.2 to 19 eV, respectively. It is worth mentioning that these energy ranges align closely with the optimal band gap of 1.4 eV for solar cell absorbers. Consequently, these compounds demonstrate a strong absorption capacity for electromagnetic waves in the Near-UV region and visible spectrum. The considerable absorptivity of electromagnetic waves within the visible spectrum and Near-UV region suggests that these compounds hold promise as potential candidates for optoelectronic applications that rely on the absorption of electromagnetic radiation within the aforementioned energy ranges.

Figure 8b illustrates the relationship between the reflectivity spectra (R) and the energy of incident electromagnetic radiation when polarized parallel to the [100], [010], and [001] crystalline directions. It is evident that the reflectivity spectra exhibit pronounced anisotropy. The magnitude of reflectivity demonstrates distinct behavior for each crystalline direction. In $LuVNi_2Sn_2$, the static value of reflectivity (R) is 44%, which gradually increases to a maximum of approximately 60% at around 1.9 eV for **E**||**a**. In $LuNbNi_2Sn_2$, the initial reflectivity is 42%, and it reaches approximately 55% at around 4 eV for E||**b**. Similarly, in $LuTaNi_2Sn_2$, the reflectivity starts at 40% and reaches approximately 55% at around 4 eV for **E**||**b**. For all three compounds, the magnitude of reflectivity (R) remains above 40% within an energy range from 0 to approximately 13 eV. Within this range, the reflectivity curve exhibits several maxima and humps, indicating complex behavior. However, for photon energies higher than approximately 13 eV, the reflectivity spectra (R) rapidly decrease and tend towards zero for all the materials studied in this research.

Figure 8c presents the predicted relationship between the refractive index ($n(\omega)$) and the energy of the incident electromagnetic radiation for three different polarizations. The refractive index exhibits some degree of anisotropy. The curve initially departs from its static value 4.96/4.63/4.45 for $LuVNi_2Sn_2$/$LuNbNi_2Sn_2$/$LuTaNi_2Sn_2$, respectively, and increases as the energy of the incident photons rises. It reaches a maximum value in the visible spectrum, specifically at approximately 6.40/5.85/5.64 for $LuVNi_2Sn_2$/$LuNbNi_2Sn_2$/$LuTaNi_2Sn_2$, respectively, at energies around 1.39/1.47/1.62 eV. Subsequently, the refractive index experiences a rapid decrease to a weak value.

3.5 Thermoelectric Properties

The present study focused on investigating the dependence of various thermoelectric coefficients on the concentration of electrons and holes at temperatures of 300 and 500 K. Specifically, the thermoelectric coefficients examined were the Seebeck coefficient (S), electrical conductivity over relaxation time (σ/τ), electronic thermal conductivity over relaxation time (k_e/τ), Pauli magnetic susceptibility parameter (χ), power factor (PF), and figure of merit (ZT). The coefficients examined were calculated including and excluding spin-orbit coupling effects. However, for the sake of complete representation and meticulous analysis, we exclusively present the results derived from the complete relativistic calculations in Fig. 9. This choice is based on two main justifications. First, the global relativistic approach incorporates the totality of interactions, thus offering an increased degree of precision in the resulting results. Second, this selection is also motivated by a deliberate aspiration for greater lucidity in presentation, a primary consideration in scientific discourse. One significant finding was that the magnitude of the Seebeck coefficient (S) for holes is greater than that for electrons in all three compounds studied. This indicates that p-type doping of the considered materials is more favorable for thermoelectric applications compared to n-type doping. The Seebeck coefficient value decreases with increasing charge carrier concentration and increases with rising temperature. Additionally, the nature of the X atom (X = V, Nb and Ta) has a minimal impact on the magnitude of the Seebeck

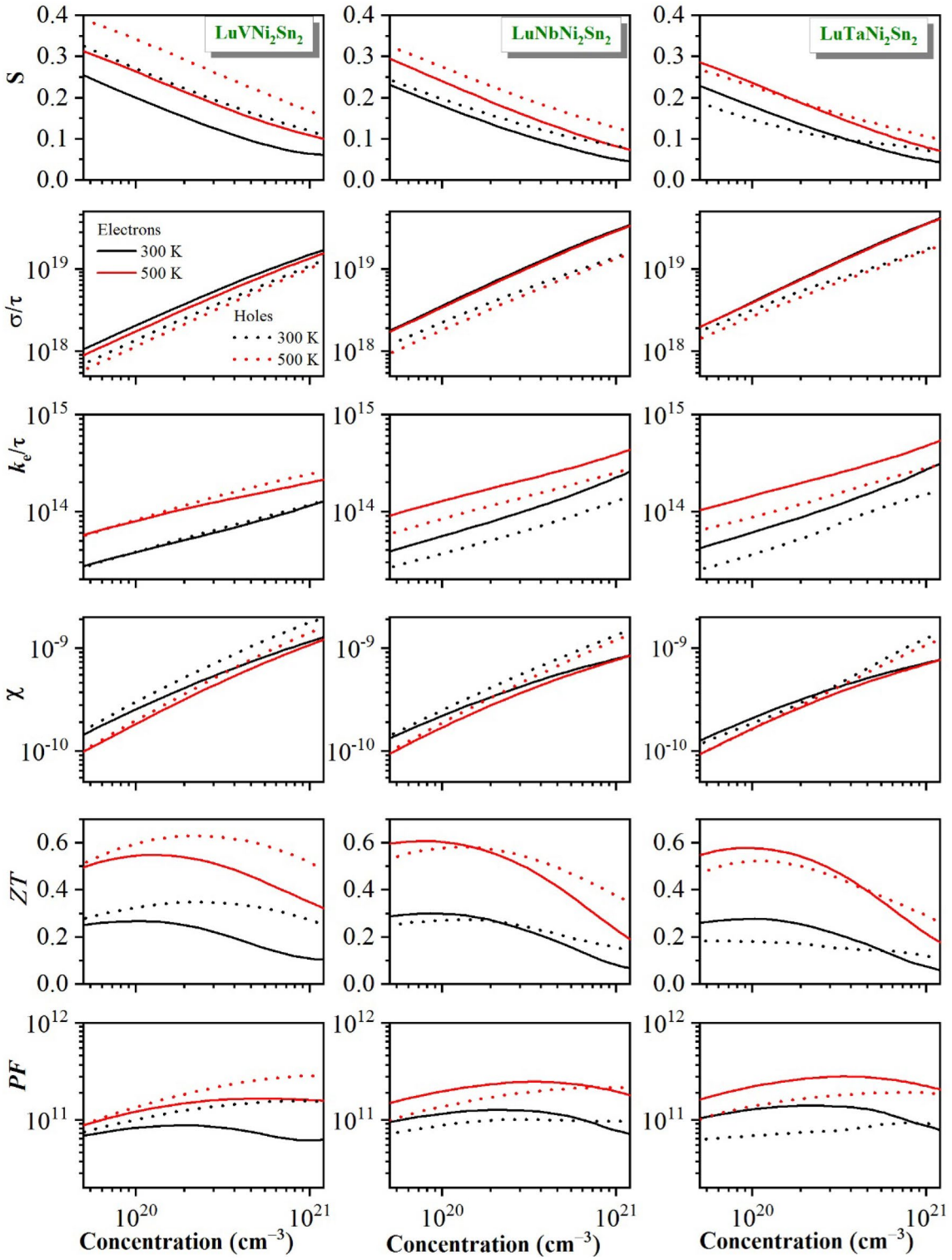

Fig. 9 Charge-carrier concentration dependence of the Seebeck coefficient (S, in mV K^{-1}), electrical conductivity over relaxation time (σ/τ, in Ω^{-1} cm^{-1} s^{-1}), electronic thermal conductivity over relaxation time (k_e/τ, in W^{-1} m^{-1} s^{-1} K^{-1}), Pauli magnetic susceptibility parameter (χ, in $m^3.mol^{-1}$) Power factor (PF, in W cm^{-1} s^{-1} K^{-2}) and figure of merit (ZT, dimensionless) at two selected temperatures T: 300 and 500 K

coefficient. Notably, $LuVNi_2Sn_2$ exhibits a higher Seebeck coefficient value compared to the other compounds at the same concentration and temperature. For example, when a temperature difference of 1 K is applied between two ends of $LuVNi_2Sn_2$, an electrical voltage of 0.25 mV could be generated. The inclusion of spin-orbit coupling only has a discernible effect in $LuTaNi_2Sn_2$ due to the larger size of the Ta atom. Analysis of the charge carrier dependence of electrical conductivity over relaxation time (σ/τ) unequivocally demonstrates the advantage of electron conductivity over holes in all three compounds. $LuVNi_2Sn_2$ exhibits slightly higher electron conductivity compared to $LuNbNi_2Sn_2$ and $LuTaNi_2Sn_2$. The study also examined the relationship between electronic thermal conductivity (k_e/τ) and charge carrier concentration at 300 and 500 K. The results indicated that the k_e/τ increases with higher temperatures and greater charge carrier concentrations, implying that a larger number of charge carriers leads to increased thermal conductivity. Notably, in $LuVNi_2Sn_2$, holes contribute somewhat more to thermal conductivity than electrons, whereas in $LuNbNi_2Sn_2$ and $LuTaNi_2Sn_2$, electrons are the dominant contributors. The Pauli magnetic susceptibility parameter (χ), which describes the behavior of conduction electrons in the presence of an external magnetic field, increases with increasing concentrations of both holes and electrons, but decreases with rising temperature.

The power factor (*PF*) is an important parameter in thermoelectric materials as it reflects the efficiency of converting temperature gradients into electrical power. $LuVNi_2Sn_2$ demonstrates the highest power factor value for a hole concentration of 10^{21} cm^{-3}. The figure of merit (*ZT*) is a crucial indicator of the overall thermoelectric performance of a material. The value of the figure of merit was calculated using the following formula : $ZT = \sigma S^2 T/(k_e + k_l)$, where S (in V K^{-1} unit) is the so-called Seebeck coefficient or thermopower, σ (in Ω^{-1} cm^{-1} unit) is the electrical conductivity, k_e and k_l are electron and lattice thermal conductivities (in W cm^{-1} K^{-1} unit), respectively, and T is the absolute temperature (in K unit). At 500 K, $LuVNi_2Sn_2$ displays the highest *ZT* value of 0.6 for a charge carrier concentration of 10^{20} cm^{-3}. This suggests that $LuVNi_2Sn_2$ possesses promising thermoelectric properties, particularly at elevated temperatures.

It should be noted that our findings underscore that the compounds examined possess a commendable figure of merit (ZT) value over the XFeSb counterparts (where X = V, Nb, and Ta), whose values remained confined within the bounds of 0.4 [48]. Notably, previous endeavors to enhance this metric through atom substitution with Hf or Ti [48] yielded minimal success. This distinction emerges due to the relatively low lattice thermal conductivity exhibited by the $LuXNi_2Sn_2$ alloys (where X = V, Nb, and Ta), attributed to their distinctive resistance to phonon propagation compared to the XFeSb counterparts (where X = V, Nb, and Ta) in their simple cubic crystal structure [48].

4 Conclusion

In this study, the properties of $LuXNi_2Sn_2$ (where X = V, Nb, and Ta) double-half Heusler alloys were investigated using density functional theory (DFT) based FP-LAPW calculations, both with and without including spin-orbit coupling. The calculations covered various aspects such as equilibrium crystal structure, thermodynamic properties, electronic structures, linear optical coefficients, and thermoelectric parameters. The equilibrium lattice parameters and atomic positions were successfully determined using the GGA-PBEsol functional, which accurately modeled the exchange-correlation energy. To confirm the thermodynamic stability of the materials, the formation enthalpy was calculated. The behavior of macroscopic thermodynamic parameters with temperature and pressure was predicted using the quasi-harmonic Debye–Slater model. By analyzing the energy band dispersions obtained from FP-LAPW calculations with the TB-mBJ potential, it was determined that the three compounds studied are semiconductors with indirect band gaps (Y–X). The density of states projected on orbitals and atoms provided insights into the electronic states composing the valence and conduction bands. It was observed that the valence band maximum (VBM) and conduction band minimum (CBM) are predominantly formed by Lu: 5*d* and X: n*d* states from the [LuX] blocks. The effective masses of charge carriers at the extremes of the energy bands were found to exhibit significant anisotropy. Linear optical coefficients were calculated for incident electromagnetic radiation polarized parallel to the [100], [010], and [001] crystal directions, revealing a noticeable anisotropy in the optical properties. The studied compounds exhibited strong absorption in the visible spectrum and near-UV region, as well as a high reflection coefficient in the visible light range. The dependence of thermoelectric properties on charge carrier concentration was investigated using Boltzmann semi-classical transport theory. Among the studied compounds, $LuNbNi_2Sn_2$ demonstrated the highest figure of merit, reaching approximately 0.6 at a charge carrier concentration of 10^{20} cm^{-3}. This indicates its favorable potential for efficiently converting heat into electricity if one is able to reduce its lattice thermal conductivity. Overall, this comprehensive analysis provides valuable insights into the structural, electronic, optical, and thermoelectric properties of $LuXNi_2Sn_2$ double-half Heusler alloys, paving the way for their potential applications in various optoelectronic and thermoelectric devices.

Acknowledgements The author S. Bin Omran acknowledges the Researchers Supporting Project Number (RSP2023R82), King Saud University, Riyadh, Saudi Arabia.

Author Contributions SSE: Conceptualization, methodology, writing and investigation, formal analysis. AB: software, verification, supervision, visualization. MEK: Conceptualization, writing. DA: Conceptualization, writing. MR: Verification, supervision. SBO: Verification, supervision. All authors have approved the final version of the manuscript.

Funding The authors have not disclosed any funding.

Declarations

Competing interest The authors declare no competing interests.

References

1. K. Bouferrache, M.A. Ghebouli, B. Ghebouli, M. Fatmi, S. Alomairy, T. Chihi, Stability, electronic band structure, magnetic, optical and thermoelectric properties of CoXCrZ (X = Fe, Mn and Z = Al, Si) and FeMnCrSb quaternary Heusler. Chin. J. Phys. **81**, 303–324 (2023)
2. M. Jamil, Q. Ain, M.U. Din, M. Yousaf, J. Munir, The structural, elastic, electromagnetic and optical response of quaternary Heusler CoFeTiZ (Z = Ge, Sb) alloys: a DFT study with mBJ and mBJ + SOC methods. Eur. Phys. J. Plus **137**, 1243 (2022). https://doi.org/10.1140/epjp/s13360-022-03454-4
3. S.S. Essaoud, A.S. Jbara, First-principles calculation of magnetic, structural, dynamic, electronic, elastic, thermodynamic and thermoelectric properties of Co_2ZrZ (Z = Al, Si) Heusler alloys. J. Magn. Magn. Mater. **531**, 167984–167999 (2021). https://doi.org/10.1016/j.jmmm.2021.167984
4. K. Boudiaf, A. Bouhemadou, Y. Al-Douri, R. Khenata, S. Bin-Omran, N. Guechi, Electronic and thermoelectric properties of the layered BaFAgCh (ch = S, Se and Te): first-principles study. J. Alloys Compd. **759**, 32–43 (2018)
5. A. Telfah, S. Sâad Essaoud, H. Baaziz, Z. Charifi, A.M. Alsaad, M.J.A. Ahmad, R. Hergenröder, R. Sabirianov, Density functional theory investigation of physical properties of KCrZ (Z = S, Se, Te) half-Heusler alloys. Phys. Status Solidi (b) **258**, 2100039 (2021)
6. D. Zou, H. Zheng, J. Li, Predicted thermoelectric properties of natural superlattice structural compounds BaCuChF (ch = S, Se and Te) by first-principles calculations. J. Alloys Compd. **686**, 571–576 (2016)
7. N.A. Koshi, R. John, Half-metallic ferrimagnetism in CoFeNbZ (Z = Al, Si, Ge, Sn) quaternary Heusler alloys: a DFT study. J. Supercond. Nov. Magn. **32**, 977–986 (2019). https://doi.org/10.1007/s10948-018-4780-y
8. I. Jum'h, S. Sâad essaoud, H. Baaziz, Z. Charifi, A. Telfah, Electronic and magnetic structure and elastic and thermal properties of Mn2-based full Heusler alloys. J. Supercond. Nov. Magn. **32**, 3915–3926 (2019). https://doi.org/10.1007/s10948-019-5095-3
9. H. Alqurashi, R. Haleoot, B. Hamad, First-principles investigations of Zr-based quaternary Heusler alloys for spintronic and thermoelectric applications. Comput. Mater. Sci. **210**, 111477 (2022)
10. J. Singh, K. Kaur, S.A. Khandy, S. Dhiman, M. Goyal, S.S. Verma, Structural, electronic, mechanical, and thermoelectric properties of LiTiCoX (X = Si, Ge) compounds. Int. J. Energy Res. **48**, 16891–16900 (2021). https://doi.org/10.1002/er.6851
11. S.A. Khandy, Inspecting the electronic structure and thermoelectric power factor of novel p-type half-Heuslers. Sci. Rep. **11**, 1–10 (2021)
12. R.K. Nutor, R. Wei, Q. Cao, X. Wang, S. Ding, D. Zhang, F. Li, J.-Z. Jiang, Quasi-superplasticity in the AlCoNiV medium entropy alloy with Heusler L21 precipitates. APL Mater. **10**, 111103 (2022)
13. M. Kratochvílová, D. Král, M. Dušek, J. Valenta, R.H. Colman, O. Heczko, M. Veis, Fe_2MnSn–experimental quest for predicted Heusler alloy. J. Magn. Magn. Mater. **501**, 166426 (2020)
14. L. Tian-Wei, C. Fu-Hua, Deformation behavior and microstructure evolution of CoCrNi medium-entropy alloy shaped charge liners. Metals 811 (2022). https://doi.org/10.3390/met12050811
15. S. Fabbrici, F. Cugini, F. Orlandi, N.S. Amadè, F. Casoli, D. Calestani, R. Cabassi, G. Cavazzini, L. Righi, M. Solzi, Magnetocaloric properties at the austenitic Curie transition in Cu and Fe substituted Ni–Mn–In Heusler compounds. J. Alloys Compd. **899**, 163249 (2022)
16. F. Cugini, S. Chicco, F. Orlandi, G. Allodi, P. Bonfá, V. Vezzoni, O.N. Miroshkina, M.E. Gruner, L. Righi, S. Fabbrici, Effective decoupling of ferromagnetic sublattices by frustration in Heusler alloys. Phys. Rev. B **105**, 174434 (2022)
17. E.C. Passamani, V.P. Nascimento, C. Larica, A.Y. Takeuchi, A.L. Alves, J.R. Proveti, M.C. Pereira, J.D. Fabris, The influence of chemical disorder enhancement on the martensitic transformation of the $Ni_{50}Mn_{36}Sn_{14}$ Heusler-type alloy. J. Alloys Compd. **509**, 7826–7832 (2011)
18. H.T. Jeong, H.K. Park, W.J. Kim, Hot deformation behavior and processing map of a $Sn_{0.5}$CoCrFeMnNi high entropy alloy with dual phases. Mater. Sci. Eng. A **801**, 140394 (2021)
19. O. Monnereau, F. Guinneton, L. Tortet, A. Garnier, R. Notonier, M. Cernea, S.A. Manea, C. Grigorescu, X-ray diffraction and microscopy investigations of structural inhomogeneities in NiMnSb crystallised from the melt. J. Phys. IV (Proc.) EDP Sci. **118**, 343–350 (2004). https://doi.org/10.1051/jp4:2004118040
20. M. Kohl, M. Gueltig, V. Pinneker, R. Yin, F. Wendler, B. Krevet, Magnetic shape memory microactuators. Micromachines **5**, 1135–1160 (2014)
21. Y. Liu, H. Xie, C. Fu, G.J. Snyder, X. Zhao, T. Zhu, Demonstration of a phonon-glass electron-crystal strategy in (Hf, Zr) NiSn half-Heusler thermoelectric materials by alloying. J. Mater. Chem. A **3**, 22716–22722 (2015)
22. T. Zhu, C. Fu, H. Xie, Y. Liu, X. Zhao, High efficiency half-Heusler thermoelectric materials for energy harvesting. Adv. Energy Mater. **5**, 1500588 (2015)
23. N. Shutoh, S. Sakurada, Thermoelectric properties of the $ti_x(Zr_{0.5}Hf_{0.5})_{1-x}$ NiSn half-Heusler compounds. J. Alloys Compd. **389**, 204–208 (2005)
24. M. Balli, S. Jandl, P. Fournier, A. Kedous-Lebouc, Advanced materials for magnetic cooling: fundamentals and practical aspects. Appl. Phys. Rev. **4**, 021305 (2017)
25. S. Chen, K.C. Lukas, W. Liu, C.P. Opeil, G. Chen, Z. Ren, Effect of Hf concentration on thermoelectric properties of nanostructured n-type half-Heusler materials $Hf_xZr_{1-x}NiSn_{0.99}Sb_{0.01}$. Adv. Energy Mater. **3**, 1210–1214 (2013)
26. N.S. Chauhan, S. Bathula, A. Vishwakarma, R. Bhardwaj, K.K. Johari, B. Gahtori, M. Saravanan, A. Dhar, Compositional tuning of ZrNiSn half-Heusler alloys: thermoelectric characteristics and performance analysis. J. Phys. Chem. Solids **123**, 105–112 (2018)
27. S. Anand, M. Wood, Y. Xia, C. Wolverton, G.J. Snyder, Double half-Heuslers. Joule. **3**, 1226–1238 (2019)
28. A. Slamani, F. Khelfaoui, O. Sadouki, A. Bentayeb, K. Boudia, F. Belkharroubi, Structural, mechanical, electronic, and thermoelectric properties of $TiZrCo_2Bi_2$, $TiHfCo_2Bi_2$, and $ZrHfCo_2Bi_2$ double half Heusler semiconductors. Emerg. Mater. 681–690 (2023). https://doi.org/10.1007/s42247-023-00468-1

29. K. Berarma, S.S. Essaoud, A.A. Mousa, S.M. Al Azar, A.Y. Al-Reyahi, Opto-electronic, thermodynamic and charge carriers transport properties of $Ta_2FeNiSn_2$ and $Nb_2FeNiSn_2$ double half-heusler alloys. Semicond. Sci. Technol. (2022). https://doi.org/10.1088/1361-6641/AC612B
30. S.S. Essaoud, A. Bouhemadou, M.E. Ketfi, D. Allali, S. Bin-Omran, Structural parameters, electronic structure and linear optical functions of $LuXCo_2Sb_2$ (X = V, Nb and Ta) double half Heusler alloys. Phys. B Condens. Matter. **657**, 414809–414819 (2023)
31. P. Blaha, K. Schwarz, F. Tran, R. Laskowski, G.K.H. Madsen, L.D. Marks, WIEN2k: an APW + lo program for calculating the properties of solids. J. Chem. Phys. **152**, 074101 (2020). https://doi.org/10.1063/1.5143061
32. J.P. Perdew, A. Ruzsinszky, G.I. Csonka, O.A. Vydrov, G.E. Scuseria, L.A. Constantin, X. Zhou, K. Burke, Restoring the density-gradient expansion for exchange in solids and surfaces. Phys. Rev. Lett. **100**, 136406 (2008). https://doi.org/10.1103/PHYSREVLETT.100.136406
33. A.D. Becke, E.R. Johnson, A simple effective potential for exchange. J. Chem. Phys. **124**, 221101 (2006). https://doi.org/10.1063/1.2213970
34. V.L.A. Otero-de-la-Roza, D. Abbasi-Pérez, Gibbs2: a new version of the quasiharmonic model code. II. Models for solid-state thermodynamics, features and implementation. Comput. Phys. Commun. **182**(10), 2232–2248 (2011)
35. V.L.A. Otero-de-la-Roza, Gibbs2: a new version of the quasi-harmonic model code. I. Robust treatment of the static data. Comput. Phys. Commun. **182**(8), 1708–1720 (2011)
36. G.K. Madsen, J. Carrete, M.J. Verstraete, BoltzTraP2, a program for interpolating band structures and calculating semi-classical transport coefficients. Comput. Phys. Commun. **231**, 140–145 (2018)
37. C. Ambrosch-Draxl, J.O. Sofo, Linear optical properties of solids within the full-potential linearized augmented planewave method. Comput. Phys. Commun. **175**, 1–14 (2006)
38. S.Z. Karazhanov, P. Ravindran, A. Kjekshus, H. Fjellvåg, B.G. Svensson, Electronic structure and optical properties of Zn X (X = O, S, Se, Te): a density functional study. Phys. Rev. B **75**, 155104 (2007). https://doi.org/10.1103/PhysRevB.75.155104
39. J.E. Saal, S. Kirklin, M. Aykol, B. Meredig, C. Wolverton, Materials design and discovery with high-throughput density functional theory: the open quantum materials database (OQMD). JOM **65**, 1501–1509 (2013)
40. S. Kirklin, J.E. Saal, B. Meredig, A. Thompson, J.W. Doak, M. Aykol, S. Rühl, C. Wolverton, The open quantum materials database (OQMD): assessing the accuracy of DFT formation energies. NPJ Comput. Mater. **1**, 1–15 (2015)
41. C.G. Broyden, The convergence of a class of double-rank minimization algorithms: 2. The new algorithm. IMA J. Appl. Math. **6**, 222–231 (1970)
42. F.D. Murnaghan, The compressibility of media under extreme pressures. Proc. Natl. Acad. Sci. USA **30**, 244 (1944)
43. A.T. Petit, P.L. Dulong, Recherches de la theorie de la chaleur. Ann. Chim. Phys. **10**, 395–413 (1819)
44. S. Sâad Essaoud, S. Al Azar, A.A. Mousa, R.S. Masharfe, Characterization of structural, dynamic, optoelectronic, thermodynamic, mechanical and thermoelectric properties of $AMgF_3$ (A = K or Ag) fluoro-perovskites compounds. Phys. Scr. **98**, 035820 (2023)
45. G.A. Slack, Nonmetallic crystals with high thermal conductivity. J. Phys. Chem. Solids **34**, 321–335 (1973)
46. A. Khireddine, A. Bouhemadou, S. Alnujaim, N. Guechi, S. Bin-Omran, Y. Al-Douri, R. Khenata, S. Maabed, A.K. Kushwaha, First-principles predictions of the structural, electronic, optical and elastic properties of the zintl-phases AE3GaAs3 (AE = Sr, Ba). Solid State Sci. **114**, 106563 (2021)
47. D.R. Penn, Wave-number-dependent dielectric function of semiconductors. Phys. Rev. **128**, 2093 (1962)
48. N.S. Chauhan, Y. Miyazaki, Iron-based semiconducting half-Heusler alloys for thermoelectric applications. ChemNanoMat. **9**, e202200403 (2023)